Atomic mixer based on phase control without ac Zeeman shift

Zhi Liang,[1] Xu-xing Geng ⬤,[1] Guo-qing Yang,[2] Kai Jin,[1] Shang-qing Liang,[2] Shao-ping Wu,[1]
Guang-ming Huang,[1,*] and Gao-xiang Li ⬤[1,†]

[1]*Department of Physics, Huazhong Normal University, Wuhan 430079, China*
[2]*College of Electronics and Information, Hangzhou Dianzi University, Hangzhou 310018, China*

Atom-based mixers have been shown to be very useful in performing the absolute measurement of the magnitude of a radio-frequency (rf) field by using Autler-Townes (AT) splitting. However, there has been less success in measuring the phase of a rf field with the AT splitting in a magnetic-resonance system. The phase of the rf magnetic field plays a very important role in imaging applications. Here, we design an atomic mixer for measuring the phase of the rf field by detecting the transmission spectra of a laser-detected magnetic-resonance system based on the interference between Raman and cascade two-photon processes for $F_g = 4$ of the D_1 line of cesium atoms. A scheme of measuring the rf phase can be realized with the elimination of the ac Zeeman shift of the system by adjusting the amplitude ratio of a transverse fundamental-wave field and its third-harmonic field. Theoretical and experimental results show that the scheme with cancellation of the ac Zeeman shift is superior in linear measurement of the longitudinal rf component. Our results provide schemes for a magnetic sensor based on quantum interference of nonlinear processes for the absolute measurement of the relative phase of rf fields.

I. INTRODUCTION

The atom-based mixer is an attractive candidate for a sensor for phase measurement of electromagnetic fields [1,2]. As a natural multiplier, an atomic mixer can generate new signals of sum frequency and difference frequency by multiplying two sinusoidal signals of different frequencies. Due to the nonlinearity of atoms, atom-based mixers have been extensively applied to measure properties including the strength [3–7], phase [8], wavelength [9], power [10], and polarization [11,12] of electromagnetic fields over a wide frequency range throughout the last decade. As a method to detect the phase of electromagnetic fields, atomic mixers have potential advantages over conventional radio technologies, which include ultrahigh-sensitivity reception with subhertz frequency resolution [13], the potential of being less susceptible to noise [14], multiband operation in one compact vapor cell [15], and the superiority of the lack of need for traditional down-conversion electronics because the atoms automatically down-convert the phase-modulated signals to an intermediate-frequency signal [16]. In the microwave domain, due to the appearance and application needs of related technologies [17–20], there is booming research into Rydberg-atom-based mixers measuring the radio-frequency (rf) phase. A prevalent way to introduce phase sensitivity is to establish the coherence between two microwave fields resonant with atoms in an electromagnetically induced transparency (EIT) system. For example, a Rydberg-atom-based system in which a local microwave field and a signal microwave field are mixed to

measure their relative phase is demonstrated in Refs. [21–23]. In such systems, the strong local field acts as a dressing field inducing Autler-Townes (AT) splitting [24] of the EIT peak, while the weak signal field acts as a probing field related to the relative phase. In addition, another popular way to introduce phase sensitivity is to establish the coherence between two resonant subsystems of multilevel atoms. For example, a class of phase-dependent microwave interferometry has been implemented in multilevel loopy ladder systems and is based upon the interference between the two subsystems [25,26]. Moreover, an internal-state Rydberg-atom interferometer for phase measurement is realized via a rf-modulated optical carrier field in a closed interferometric loop [27]. In such systems, the phase dependency of the EIT signal is induced by the quantum interference between the closed interferometric loops formed by subsystems. Owing to large-transition dipole moments between energetically adjacent Rydberg states, Rydberg-atom-based mixers have been widely studied in the phase measurements of rf electric field in the gigahertz band. However, in the kilohertz-band rf domain, less attention has been paid to the atom-based mixer for characterizing magnetic-field properties, especially in using magnetic resonance to measure the phase of a rf field. Although the preparation of atomic states and the coupling mode between atoms and electromagnetic fields in the magnetic-resonance system are completely different from those in the EIT system, the two systems are consistent in the way they characterize the strength and phase of electromagnetic fields via laser-detected AT spectra. That is, the two systems can measure the field strength by dressing the atom with a strong field and probing the system with a weak field and introduce phase sensitivity via the coherence between fields. In view of the significance of the phase of the rf magnetic field in
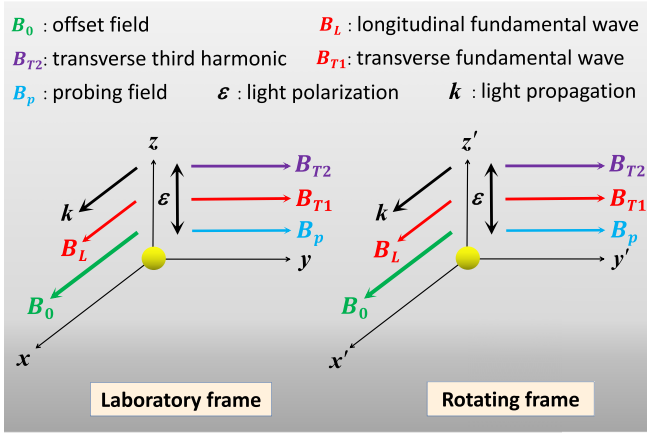
*gmhuang@ccnu.edu.cn
†gaox@ccnu.edu.cn

FIG. 1. Theoretical model geometry of the system in a laboratory frame xyz where the quantization axis lies along the direction of light polarization ε and in a rotating frame $x'y'z'$ where the quantization axis lies along the direction of the offset field B_0.

FIG. 2. Schematic of two-photon transition processes. The Zeeman splitting caused by the offset field is Ω_0, and the ac Zeeman shift caused by the transverse rf fields is $\Delta\Omega_0$. The left section indicates that when the condition $\omega_{\sigma(\pi)} - \omega_{\pi(\sigma)} = \Omega_0 + \Delta\Omega_0$ is met, the atoms in the ground-state sublevels will absorb a σ (or π) rf photon and then release a π (or σ) rf photon to form a Raman two-photon process. The right section indicates that when the condition $\omega_\sigma + \omega_\pi = \Omega_0 + \Delta\Omega_0$ is met, the atoms in the ground-state sublevels will absorb a π rf photon and a σ rf photon to form a cascade two-photon process.

practical applications [28–34], the phase measurement of a rf magnetic field by an atomic mixer would be interesting. As rf magnetic resonance occurs in the hyperfine energy levels of atoms, an atomic mixer based on a magnetic-resonance system can realize the phase measurement of the rf magnetic field in the low-frequency and even very-low-frequency band. Moreover, due to the narrow ground-state linewidth of the atoms housed in a paraffin-coated cell, AT splitting based on magnetic resonance is more advantageous in the phase measurement for a weak rf magnetic field. A phase-controlled atomic mixer based on the interference between Raman and cascade two-photon processes can be realized with two schemes, as we will discuss.

In this paper, two magnetic-resonance schemes for realizing an atomic mixer based on the interference between Raman and cascade two-photon processes for $F_g = 4$ of the D_1 line of cesium atoms are proposed. Nevertheless, Raman or cascade two-photon processes will inevitably cause ac Zeeman shifts [35] of the system. For the scheme with only one transverse rf field participating in two-photon resonances, the ac Zeeman shift of the system cannot be completely canceled. But for the scheme with two transverse rf fields, the ac Zeeman shift can be eliminated by stabilizing a specific amplitude ratio between transverse rf fields. This manner of eliminating energy-level shift by setting a specific ratio of physical quantities has been applied in the study of dual-color magic-wavelength traps for the suppression of atomic ac Stark shifts [36]. In our discussion, a scheme in which the elimination of the ac Zeeman shift of the system can be achieved, labeled scheme I, is mainly discussed. In Sec. II, we describe the theoretical model of scheme I, which is depicted in Fig. 1, and derive the Hamiltonian of the system in the dressed-state representation. Then the second-order perturbation solution of the AT spectrum of the system is given. In Sec. III, we introduce the experimental setup of scheme I and demonstrate the effects of different transverse rf components on the ac Zeeman shift of the system and the sideband interval of the AT doublet. Subsequently, the relationship between the sideband interval and the relative phase is investigated. And the linear relationship between the
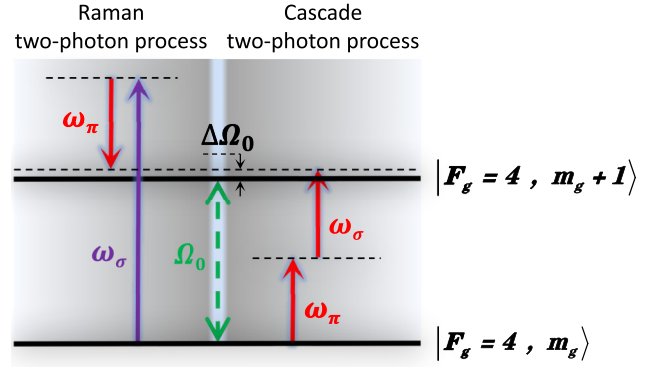
longitudinal Rabi frequency and the sideband interval is evaluated under different relative phases. For comparison, another scheme in which the ac Zeeman shift cannot be eliminated, labeled scheme II, is detailed in Appendix C. Finally, we make a conclusion in Sec. IV.

II. THEORY

A. Theoretical model

Magnetic resonance based on two-photon transition with $\Delta m = \pm 1$ is coexcited by two orthogonal rf fields [37,38]. Consider a magnetic-resonance system in which a longitudinal fundamental-wave field participates in both Raman and cascade two-photon processes, where the geometry of the magnetic fields is shown in Fig. 1. Two rf fields with the same frequency as fundamental-wave fields are set orthogonally, wherein the rf field parallel to the offset field generates the longitudinal component of the fundamental-wave fields and the rf field perpendicular to the offset field generates the transverse component. As shown in Fig. 2, the longitudinal fundamental-wave field can cause a Raman two-photon process together with a transverse third-harmonic field, on the one hand, and can cause a cascade two-photon process together with a transverse fundamental-wave field, on the other hand. The Raman and cascade two-photon processes are generated simultaneously and interfere with each other. The resulting interference field acts as a strong driving field to dress the ground-state sublevels of atoms. In the dressed-state system coupled to a strong driving field, an AT doublet can be used to achieve the absolute-magnitude measurement of the driving field [39,40]. With two-photon resonance, the interference intensity of these two nonlinear processes has a linear relationship with the sideband interval of the AT doublet.

We consider the magnetic-resonance geometry of Fig. 1, where two transverse rf magnetic fields, $\boldsymbol{B}_{T1} = B_{T1}\cos(\omega t +$

$\varphi)\mathbf{e}_{x'}$ and $\mathbf{B}_{T2} = B_{T2}\cos(3\omega t + \theta)\mathbf{e}_{x'}$, are perpendicular to the offset field $\mathbf{B}_0$, while another longitudinal rf magnetic field, $\mathbf{B}_L = B_L\cos(\omega t + \varphi)\mathbf{e}_{z'}$, is parallel to $\mathbf{B}_0$. In this geometry, the orientation $\mathbf{k}$ of linearly polarized light is along the direction of $\mathbf{B}_0$, and the light polarization $\boldsymbol{\varepsilon}$ is perpendicular to all the magnetic fields. Our discussion of laser-detected magnetic resonance follows the three-step approach [41–43], which includes polarization-state preparation [44,45], magnetic resonance [46,47], and optical detection [48,49]. In the preparation process of our system, atomic alignment is created by the linearly polarized light which resonates with the sublevels in the ground state $F_g = 4$ and the excited state $F_e = 3$ of the D_1 line of cesium atoms, and the alignment is described in a laboratory frame xyz, where the quantization axis lies along the direction of $\boldsymbol{\varepsilon}$ shown in Fig. 1. In the process of magnetic resonance, the atoms in the ground-state sublevels absorb the rf photons generated by the transverse and longitudinal fields and transit to the neighboring sublevels; that is, the magnetic resonance excited by the rf fields is a two-photon process. When the equivalent Larmor precession frequencies produced by the two-photon processes match the sum of the Zeeman splitting Ω_0 and the ac Zeeman shift $\Delta\Omega_0$, the Raman two-photon magnetic resonance and the cascade two-photon magnetic resonance are excited, as shown in Fig. 2. In the optical detection process, the magnetic resonance induced by the rf fields changes the atomic alignment. When the repopulation process of the ground-state atoms induced by the light reaches a balance with the magnetic-resonance process, the information about the field-atom interaction can be obtained by measuring the transmission spectrum [50]. Moreover, to probe the magnetic-resonance process, a weak rf magnetic field $\mathbf{B}_p$ is introduced transversely for probing.

B. Hamiltonian of the system

Our system is studied in the rotating frame $x'y'z'$ shown in Fig. 1. The Hamiltonian in Cartesian representation is given by $H_B = \mu_B g_F(F_{x'}B_{x'} + F_{y'}B_{y'} + F_{z'}B_{z'})$, where μ_B, g_F, $F_{i'}$, and $B_{i'}$ $(i = x, y, z)$ are the Bohr magneton, the Landé factor, the angular momentum component, and the magnetic-field component in the Cartesian representation, respectively. According to the relation between Cartesian and spherical basis vectors [51], the total magnetic-field–atom interaction Hamiltonian in the bare-state representation is given by

$$H_{B_{\text{tot}}} = H_{B_m} + H_{B_p}, \tag{1}$$

with

$$H_{B_m} = [\Omega_0 + \Omega_L\cos(\omega t + \varphi)]F_0$$
$$+ \left[\frac{\Omega_{T1}}{\sqrt{2}}\cos(\omega t + \varphi) + \frac{\Omega_{T2}}{\sqrt{2}}\cos(3\omega t + \theta)\right]F_{-1}$$
$$- \left[\frac{\Omega_{T1}}{\sqrt{2}}\cos(\omega t + \varphi) + \frac{\Omega_{T2}}{\sqrt{2}}\cos(3\omega t + \theta)\right]F_{+1}, \tag{2}$$

$$H_{B_p} = \frac{\Omega_p}{\sqrt{2}}\cos(\omega_p t)(F_{-1} - F_{+1}). \tag{3}$$

Here, H_{B_m} is the main magnetic-field–atom interaction Hamiltonian. H_{B_p} is the probing magnetic-field–atom interaction

Hamiltonian, and ω_p is the angular frequency of $\mathbf{B}_p$. The symbol satisfies $\Omega_j = \mu_B g_F B_j$ $(j = 0, L, T1, T2, p)$, where Ω_0, Ω_L, Ω_{T1}, Ω_{T2}, and Ω_p are the Zeeman splitting and the Rabi frequencies of longitudinal field B_L, transverse fields B_{T1} and B_{T2}, and probing field B_p, respectively. The operator $F_\mu(\mu = 0, \pm 1)$ is the angular momentum operator in the covariant spherical basis representation. Considering the conditions 3ω, $|\Omega_0 - \omega| \gg \Omega_{T1}, \Omega_{T2}$ and the restriction that ω and 3ω are far detuned from Ω_0, the effective Hamiltonian of H_{B_m} can be derived from James's effective Hamiltonian theory [52,53] and is given by

$$H_{B_m}^{\text{eff}} \approx \Delta\Omega_0 F_0$$
$$+ [\Omega_R e^{i(\delta t + \theta - \varphi)} - \Omega_C e^{i(\delta t + 2\varphi)}]F_{-1}$$
$$- [\Omega_R e^{-i(\delta t + \theta - \varphi)} - \Omega_C e^{-i(\delta t + 2\varphi)}]F_{+1}, \tag{4}$$

with

$$\Delta\Omega_0 = \frac{\Omega_0}{4}\left(\frac{\Omega_{T1}^2}{\Omega_0^2 - \omega^2} + \frac{\Omega_{T2}^2}{\Omega_0^2 - 9\omega^2}\right),$$
$$\Omega_R = \frac{\Omega_L\Omega_{T2}}{4\sqrt{2}\omega}, \quad \Omega_C = \frac{\Omega_L\Omega_{T1}}{4\sqrt{2}\omega}. \tag{5}$$

Here, the coefficient $\Delta\Omega_0$ is the ac Zeeman shift [35], which represents the energy shift of the magnetic sublevels. For $\Delta\Omega_0 \neq 0$, the decrease or increase of the separation between adjacent magnetic sublevels corresponds to the redshift or blueshift of the resonant frequency. Under the resonance condition, there exists an amplitude ratio between Ω_{T1} and Ω_{T2} that keeps $\Delta\Omega_0$ canceled. The amplitude ratio satisfies $\Omega_{T1}/\Omega_{T2} = \sqrt{3/5}$, which guarantees that the redshift caused by $\mathbf{B}_{T2}$ and the blueshift caused by $\mathbf{B}_{T1}$ cancel each other so that the overall ac Zeeman shift is eliminated. The coefficients Ω_R and Ω_C are the equivalent Rabi frequencies of the Raman and cascade two-photon processes, respectively. The symbol $\delta = 2\omega - \Omega_0$ uniformly represents the frequency detuning between the Raman or cascade two-photon process and the Zeeman splitting.

To gain further insight, the total Hamiltonian $H_{B_{\text{tot}}}$ is discussed in the dressed-state representation. The effective Hamiltonian $H_{B_m}^{\text{eff}}$ can be diagonalized. The eigenvectors of the effective Hamiltonian after diagonalization act as state vectors in the dressed-state representation. In the dressed-state representation, each ground-state sublevel is dressed to nine sublevels with equal splitting Ω, i.e., the so-called AT splitting [54], which is given by

$$\Omega = \sqrt{\Omega_z^2 + 2(\Omega_R^2 + \Omega_C^2 - 2\Omega_R\Omega_C\cos\Delta\phi)}. \tag{6}$$

Here, $\Omega_z = \Delta\Omega_0 - \delta$ is the detuning of two-photon processes, and $\Delta\phi = \theta - 3\varphi$ is the relative phase. Equation (6) indicates that the phase information of the main rf fields is transferred to the sublevel splitting in the dressed-state representation. The splitting width is periodically controlled by $\Delta\phi$. With the two-photon resonance condition $2\omega = \Omega_0 + \Delta\Omega_0$, the splitting width can linearly reflect the interference intensity between Raman and cascade two-photon processes. Moreover, the splitting has a linear relationship with the longitudinal rf component of the system at any $\Delta\phi$. The total Hamiltonian

in the dressed-state representation is given by

$$
\begin{aligned}
H_{B_{\text{tot}}}^{(d)} = {} & \frac{\Omega_p}{4}\sin\beta(e^{i\delta_p t} + e^{-i\delta_p t})F_0^{(d)} \\
& + \frac{\Omega_p}{4\sqrt{2}}(1+\cos\beta)\left[e^{i(\delta_p-\Omega)t}F_{-1}^{(d)} - e^{-i(\delta_p-\Omega)t}F_{+1}^{(d)}\right] \\
& + \frac{\Omega_p}{4\sqrt{2}}(1-\cos\beta)\left[e^{i(\delta_p+\Omega)t}F_{+1}^{(d)} - e^{-i(\delta_p+\Omega)t}F_{-1}^{(d)}\right].
\end{aligned}
\tag{7}
$$

Here, $\delta_p = \omega_p - 2\omega$ is the detuning between the probing field and the Raman or cascade two-photon process. The operator $F_\mu^{(d)}(\mu = 0, \pm 1)$ is the angular momentum operator in the dressed-state representation. The angle β is the Euler angle, which satisfies $\cos\beta = \Omega_z/\Omega$ and $\sin\beta = \sqrt{2(\Omega_R^2 + \Omega_C^2 - 2\Omega_R\Omega_C\cos\Delta\phi)}/\Omega$. A detailed derivation of Eq. (7) is given in Appendix A. In the dressed-state representation, the total magnetic-field–atom interaction Hamiltonian can be written into the rotating frame with frequency Ω, in which the main rf fields determine the center frequency and the sideband interval of the transmission spectrum. After scanning the probing field, three kinds of transitions corresponding to the resonant frequencies $2\omega - \Omega$, 2ω, and $2\omega + \Omega$ appear. However, only transitions with $2\omega \pm \Omega$ cause changes in atomic alignment [55]. The two sidebands are known as the AT doublet response with a center frequency of 2ω and a span of 2Ω.

C. Transmission spectrum of the system

In our system, considering the weak pumping intensity of linearly polarized light, the multipole moments of the ground-state atoms can be reduced to second order. According to [43,56–58], the absorption coefficient α of the system in the laboratory frame xyz can be expanded using multipole moments as

$$
\alpha = \alpha_0(14m_{0,0} - \sqrt{77}m_{2,0}),
\tag{8}
$$

where α_0 is a constant. The monopole moment $m_{0,0}$ is a coefficient linearly related to the total population of the ground-state atoms. The multipole moment $m_{2,0}$ describes the atomic alignment. Under the condition of steady state, $m_{0,0}$ is a constant, while $m_{2,0}$ is the only dependent factor of the absorption coefficient. The time-independent component of $m_{2,0}$ in the laboratory frame xyz is given by

$$
m_{2,0}^{(\text{dc})} = \frac{3\cos^2\beta - 1}{4}\left\{ \frac{\Gamma_0}{3\gamma_0} - \frac{\Gamma_0\gamma_1\Omega_p^2}{16\gamma_0^2}\left[\frac{(1-\cos\beta)^2}{\gamma_1^2 + (\delta_p+\Omega)^2} \right.\right.
$$
$$
\left.\left. + \frac{(1+\cos\beta)^2}{\gamma_1^2 + (\delta_p-\Omega)^2} \right] \right\}.
\tag{9}
$$

Here, $m_{2,0}^{(\text{dc})}$ represents the dc signal of the magnetic-resonance transmission spectrum in the laboratory frame xyz. The coefficients Γ_0, γ_0, and γ_1 are the alignment relaxation rates related to the optical pump relaxation process and the ground-state spin-exchange collision relaxation process of the system. A detailed derivation of Eq. (9) is given in Appendix B. Equation (9) indicates that the AT doublet appears when the
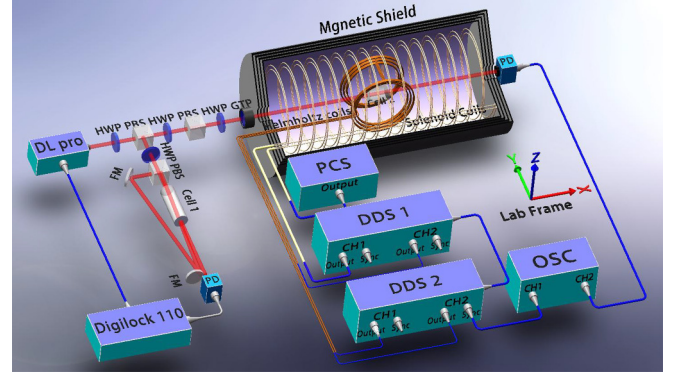

FIG. 3. Experimental setup. DL pro, grating-stabilized tunable single-mode diode laser; HWP, half-wave plate; PBS, polarization beam splitter; FM, flat mirror; Digilock 110, feedback controller Digilock 110; GTP, Glan-Taylor prism; cell 1, vacuum chamber filled with cesium atoms; cell 2, cesium atomic cell coated with paraffin; PD, photodetector; DDS, direct digital frequency synthesizer; PCS, precision current source; OSC, digital storage oscilloscope. All details can be found in the text.

probing field meets the resonance condition. The AT spectrum of the magnetic resonance based on the interference between Raman and cascade two-photon processes has properties similar to that based on a single-photon processes [55]. The distinction between them is that the relative phase $\Delta\phi$ between Raman and cascade two-photon processes can determine the AT splitting and realize periodic control of the sideband interval of the AT doublet. However, this phase-controlled regulation of AT splitting cannot be realized in the magnetic resonance based on a single two-photon process (Raman or cascade) or a single-photon process. In addition, since Raman two-photon resonance modes are not unique, there are two schemes for realizing the AT spectrum of magnetic resonance based on the interference between Raman and cascade two-photon processes. Particularly, the scheme involving two transverse rf fields can realize the cancellation of the ac Zeeman shift by stabilizing a specific amplitude ratio between the two transverse rf fields.

III. EXPERIMENT

A. Experimental setup

The experimental setup of the system in Fig. 1 is mainly composed of the optical part and the circuit-instrument part, as schematically shown in Fig. 3. For the optical part, a Toptica DL pro 894-nm laser is used as the light source. The laser beam from the beginning is split into two subbeams: one subbeam is used for saturated absorption frequency stabilization [59], while the other subbeam is used for the magnetic resonance. A Toptica Digilock 110 is utilized to implement the frequency lock with an accuracy of about 500 kHz in the experiment. The linearly polarized light prepares cesium atoms with an incident power of about 25 μW with a spot diameter of 5 mm and then is received by a photodetector (Newport optical receiver 2031). The atoms used are a cesium atomic vapor housed in a cylindrical and paraffin-coated cell with a length of 30 mm and diameter of 25 mm (cell 2 in Fig. 3).

For the circuit instrument part, two direct digital frequency synthesizers (DDSs) with double output channels (RIGOL DG4062 and RIGOL DG4162) are used as the excitation sources for generating rf magnetic fields. To ensure the coherence between the main rf magnetic fields, the synchronous output of DDS1 is used as the external clock source of DDS2. The transverse rf fields are generated by three pairs of Helmholtz coils driven by DDS1 and DDS2. Helmholtz coils with an average diameter of 88 mm are wound with equal turns at an inclination angle of $63.4°$ on a 3D-printed mold. The longitudinal rf field is generated by the outer solenoid coils driven by DDS1, while the offset field is generated by the inner solenoid coils driven by a precision current source (Keysight B2912A). As shown in Fig. 3, the transverse field and longitudinal field of the rf fundamental wave are output by two channels of DDS1 set in the same phase, while the transverse third-harmonic field is output by one channel of DDS2 and the transverse probing field is output by another channel of DDS2. Because the clocks of DDS2 and DDS1 are synchronized, the step control of the relative phase can be realized by setting the phase step of the transverse third-harmonic field. To isolate the system from environmental magnetic fields in the laboratory, the solenoids with Helmholtz coils are placed in a magnetic shield with four layers of μ-metal cylinders, whose fluctuation of magnetic field in the middle zone is about 2 nT/cm when the offset field is about 50 000 nT. The dc component is filtered out and amplified from the magnetic-resonance signal received by the photodetector before being input to the digital storage oscilloscope.

In our experiment, the Rabi frequencies of rf fields need to be calibrated and determined. The transverse rf field is generated by a standard Helmholtz coil, and its Rabi frequency can be measured via the AT splitting of magnetic-resonance spectra dressed by a rf field [55]. The longitudinal rf field is generated by a standard solenoid coil, and its Rabi frequency can be calibrated and measured via AT splitting of magnetic-resonance spectra dressed by a single rf two-photon process [38].

B. Experimental results and analyses

We first explore the magnetic-resonance AT spectrum of the system with different ac Zeeman shifts and verify the relationship between the sideband interval and the relative phase under the condition that the ac Zeeman shift is about 0 Hz. Then the relationship between the sideband interval and the longitudinal rf component is investigated under the condition of two different relative phases.

According to Eq. (5), under the premise of $\Omega_0 \gg \Delta\Omega_0$ and the resonance condition, $\Delta\Omega_0$ can be approximately considered to be related to only the amplitudes of the transverse rf fields. In our experiment, $\Omega_0 = 2\pi \times 100.161$ kHz is the center frequency obtained from the magnetic resonance excited only by the transverse probing field $\boldsymbol{B}_p$. As shown in Fig. 4, the longitudinal Rabi frequency $\Omega_L = 2\pi \times 6.236(5)$ kHz and the transverse Rabi frequency $\Omega_{T2} = 2\pi \times 12.910(5)$ kHz remain unchanged, and the settings for the transverse Rabi frequency Ω_{T1} are $2\pi \times 9.223(5)$, $2\pi \times 9.992(5)$, and $2\pi \times 10.711(5)$ kHz, corresponding to ac Zeeman shifts of about -50, 0, and 50 Hz, respectively. There
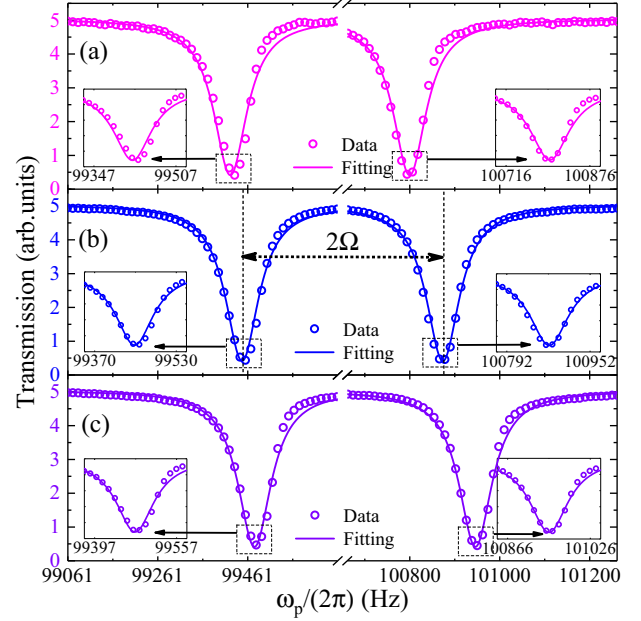

FIG. 4. AT spectra vs the frequency of the probing field $\boldsymbol{B}_p$. (a) The pink circles represent the measured data of $\frac{\Delta\Omega_0}{2\pi} \approx -50$ Hz; the resonant frequencies of the left and right sidebands are about 99 427 and 100 796 Hz, respectively. (b) The blue circles represent the measured data of $\frac{\Delta\Omega_0}{2\pi} \approx 0$ Hz; the resonant frequencies of the left and right sidebands are about 99 450 and 100 872 Hz, respectively. (c) The purple circles represent the measured data of $\frac{\Delta\Omega_0}{2\pi} \approx 50$ Hz; the resonant frequencies of the left and right sidebands are about 99 477 and 100 946 Hz, respectively. All data are measured under the condition of $\Delta\phi = \pi$. The fitting curves are the line shapes with $\gamma_1 \approx 2\pi \times 45$ Hz from Eq. (9).

are three kinds of ac Zeeman shifts. With $\Omega_{T1}/\Omega_{T2} < \sqrt{3/5}$, the blueshift caused by $\boldsymbol{B}_{T1}$ is weaker than the redshift caused by $\boldsymbol{B}_{T2}$, and the overall shift effect of the ground-state sublevels behaves as a redshift, corresponding to the situation in which the center frequency of the AT doublet is less than the Larmor precession frequency Ω_0, as shown in Fig. 4(a). With $\Omega_{T1}/\Omega_{T2} = \sqrt{3/5}$, the blueshift equals the redshift, so the ac Zeeman shift is canceled, corresponding to the situation in which the center frequency of the AT doublet locates at Ω_0, as shown in Fig. 4(b). With $\Omega_{T1}/\Omega_{T2} > \sqrt{3/5}$, the blueshift surpasses the redshift, and the overall shift effect behaves as a blueshift, corresponding to the situation in which the center frequency of the AT doublet is more than Ω_0, as shown in Fig. 4(c).

Figure 5 shows that the mixing process based on the interference of Raman and cascade two-photon processes is controlled by the relative phase $\Delta\phi$. According to Eq. (4), the phase felt by atoms in the Raman process is the phase difference of $\boldsymbol{B}_{T2}$ and $\boldsymbol{B}_L$, i.e., $(\theta - \varphi)$, and that in the cascade process is the phase sum of $\boldsymbol{B}_{T1}$ and $\boldsymbol{B}_L$, i.e., 2φ. Since the Raman two-photon process and the cascade two-photon process resonate in the same sublevel frame, the mixing process of the two different nonlinear resonant processes can be analogous to that of two monochromatic waves with phases $(\theta - \varphi)$ and 2φ, respectively. AT splitting dressed only by a Raman or cascade two-photon process cannot be regulated by the
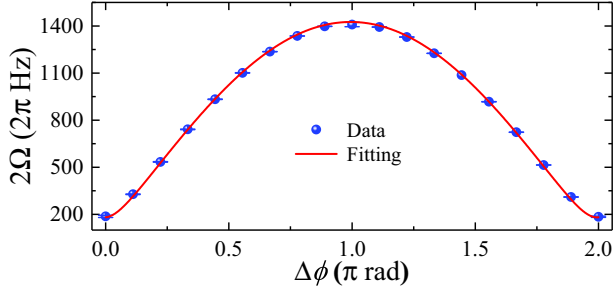
FIG. 5. Sideband interval vs relative phase. The blue solid dots represent the measured data with a step of $\pi/9$. All data are measured under the resonance condition with $\Omega_0 = 2\pi \times 100.161 \, \text{kHz}$, $\Omega_L = 2\pi \times 6.236(5) \, \text{kHz}$, $\Omega_{T1} = 2\pi \times 9.992(5) \, \text{kHz}$, and $\Omega_{T2} = 2\pi \times 12.910(5) \, \text{kHz}$. The red fitting curve is the theoretical fit of Eq. (6).

phase of the single nonlinear process. The phase control of AT splitting must be on the basis of two distinct two-photon processes in cooperation.

In the scheme in Fig. 1, the longitudinal rf field $\boldsymbol{B}_L$ participates in both Raman and cascade two-photon process. According to Eqs. (5) and (6), under the resonance condition, the longitudinal Rabi frequency Ω_L acts on the AT splitting Ω as a linear term and is not affected by the relative phase. Under the condition of two different relative phases, the relationship between the sideband interval and Ω_L shows good linearity, as shown in Fig. 6.

IV. CONCLUSION

In this paper, a scheme for realizing an atomic mixer based on the interference between Raman and cascade two-photon processes was studied theoretically and experimentally. The scheme was implemented on a laser-detected magnetic-resonance system for $F_g = 4$ of the D_1 line of cesium atoms, and the absolute measurement for the relative phase between the fundamental-wave fields and a third-harmonic field was
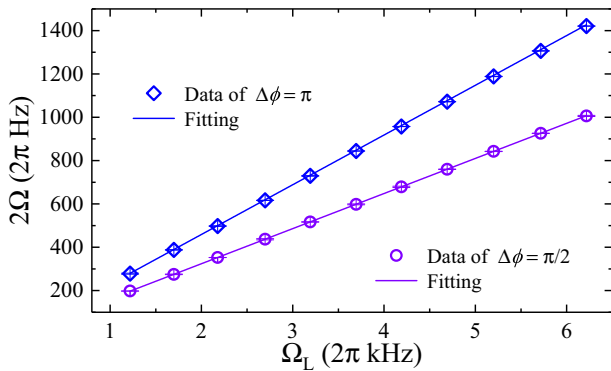

FIG. 6. Sideband interval vs longitudinal Rabi frequency. The blue diamonds represent the measured data with $\Delta\phi = \pi$; the purple circles represent the measured data with $\Delta\phi = \pi/2$. All data are measured under the same resonance condition with $\Omega_0 = 2\pi \times 100.161 \, \text{kHz}$, $\Omega_L = 2\pi \times 6.236(5) \, \text{kHz}$, $\Omega_{T1} = 2\pi \times 9.992(5) \, \text{kHz}$, and $\Omega_{T2} = 2\pi \times 12.910(5) \, \text{kHz}$. The fitting curves are the theoretical fits of Eq. (6).

achieved by detecting the transmission spectra of the system. The Raman and cascade two-photon processes mix in the same resonance frame of the atomic ground state and form an interference field to dress the ground-state sublevels. By scanning the probing field, the AT spectra of the magnetic-resonance system can be obtained. The sideband interval of the AT doublet of the system is regulated by the relative phase between the rf harmonics. Moreover, the sideband interval of the AT doublet is linearly related to the longitudinal fundamental-wave field with the two-photon resonance at any relative phase.

Due to the opposite directions of the ac Zeeman shifts caused by the transverse fundamental-wave field and its third-harmonic field, scheme I discussed above can realize the elimination of the total ac Zeeman shift of the system by stabilizing a specific amplitude ratio of the two transverse rf fields. If the direction of the third-harmonic field in the above scheme is changed from transverse to longitudinal, the system can still construct the interference field of two Raman and cascade two-photon processes and realize the atomic mixer based on phase control as well. However, the ac Zeeman shift of the system cannot be completely eliminated with only one transverse rf field. In addition, in scheme II, which has only one transverse rf field, only under certain relative phase values can the AT splitting of the system be linear with the amplitude of the longitudinal rf field. Scheme II is detailed in Appendix C.

APPENDIX A: DERIVATION OF EQUATION (7)

The angular momentum operators in the bare-state and dressed-state representations are defined by

$$F_\mu = \sum_m 2\sqrt{5} C_{4m1\mu}^{4m+\mu} |m+\mu\rangle\langle m|,$$

$$F_\mu^{(d)} = \sum_{m^{(d)}} 2\sqrt{5} C_{4m^{(d)}1\mu}^{4m^{(d)}+\mu} |m^{(d)}+\mu\rangle\langle m^{(d)}|, \quad \text{(A1)}$$

respectively. Here, $|m+\mu\rangle\langle m|$ and $|m^{(d)}+\mu\rangle\langle m^{(d)}|$ (m, $m^{(d)} = -4, \ldots, 4$) are the transition operators in the bare-state and dressed-state representations, respectively. $C_{\cdots}^{[\cdot\cdot]}$ is the Clebsch-Gordan coefficient of $F_g = 4$. Since the main magnetic-field–atom interaction Hamiltonian H_{B_m} dominates the evolution of the system's transmission spectrum, the effective Hamiltonian $H_{B_m}^{\text{eff}}$ can be performed on the diagonalization operation in the frequency-rotating frame of frequency δ, specifically,

$$\left(e^{i\delta F_0 t} H_{B_m}^{\text{eff}} e^{-i\delta F_0 t}\right) |m^{(d)}\rangle = \lambda |m^{(d)}\rangle. \quad \text{(A2)}$$

Here, $e^{-i\delta F_0 t}$ is the rotating operator with frequency δ in the bare-state representation. The eigenvalue satisfies $\lambda = m^{(d)}\Omega$, where Ω is the splitting of the neighboring dressed-state sublevels, which is given by Eq. (6). The state vector $|m^{(d)}\rangle$ is the eigenvector in the dressed-state representation, which is given

by

$$|m^{(d)}\rangle = \sum_m \left[D^{(4)}_{mm^{(d)}}(\beta) \right]^* |m\rangle, \tag{A3}$$

where function $D^{(4)}_{mm^{(d)}}(\beta)$ is the Wigner D function [51] with the Euler angle β, which satisfies $\cos \beta = \Omega_z / \Omega$ and $\sin \beta = \sqrt{2(\Omega_R^2 + \Omega_C^2 - 2\Omega_R \Omega_C \cos \Delta\phi)}/\Omega$. According to Eqs. (A1) and (A3), the relation of the angular momentum operators between the bare-state representation and the dressed-state representation is given by

$$F_0 = \cos\beta F_0^{(d)} + \frac{\sin\beta}{\sqrt{2}} F_{+1}^{(d)} - \frac{\sin\beta}{\sqrt{2}} F_{-1}^{(d)},$$

$$F_{+1} = -\frac{\sin\beta}{\sqrt{2}} F_0^{(d)} + \frac{1+\cos\beta}{2} F_{+1}^{(d)} + \frac{1-\cos\beta}{2} F_{-1}^{(d)},$$

$$F_{-1} = \frac{\sin\beta}{\sqrt{2}} F_0^{(d)} + \frac{1-\cos\beta}{2} F_{+1}^{(d)} + \frac{1+\cos\beta}{2} F_{-1}^{(d)}. \tag{A4}$$

According to Eqs. (1)–(3) and (A4), The total magnetic-field–atom interaction Hamiltonian in the dressed-state representation is given by Eq. (7).

APPENDIX B: DERIVATION OF EQUATION (9)

In the dressed-state representation, the master equation for the evolution of the systematic density matrix is

$$\dot{\rho}^{(d)} = -i\left[H_{B_{\text{tot}}}^{(d)}, \rho^{(d)} \right] + \mathcal{L}_\rho^{(d)}, \tag{B1}$$

where $\mathcal{L}_\rho^{(d)}$ represents the systematic relaxation process in the dressed-state representation. According to the theory of state multipoles [60], the density-matrix element $\rho^{(d)}$ can be expressed in the representation of multipole moments $m_{k,q}^{(d)}$ through a set of complete irreducible tensor bases $T_{k,q}^{(d)}$, i.e., $\rho^{(d)} = \sum_{k=0}^{2F} \sum_{q=-k}^{k} m_{k,q}^{(d)} T_{k,q}^{(d)}$. Then the evolution of atomic second-order multipole moments takes the following form:

$$\dot{m}_{2,-2}^{(d)} = (2i\xi_0 + \gamma_2)m_{2,-2}^{(d)} - \sqrt{2}i\xi_{-1}m_{2,-1}^{(d)},$$

$$\dot{m}_{2,-1}^{(d)} = (i\xi_0 + \gamma_1)m_{2,-1}^{(d)} + \sqrt{2}i\xi_{+1}m_{2,-2}^{(d)} - \sqrt{3}i\xi_{-1}m_{2,0}^{(d)},$$

$$\dot{m}_{2,0}^{(d)} = \gamma_0 m_{2,0}^{(d)} + \sqrt{3}i\xi_{+1}m_{2,-1}^{(d)} - \sqrt{3}i\xi_{-1}m_{2,1}^{(d)} + \Gamma_0 m_{0,0}^{(d)},$$

$$\dot{m}_{2,1}^{(d)} = (-i\xi_0 + \gamma_1)m_{2,1}^{(d)} - \sqrt{2}i\xi_{-1}m_{2,2}^{(d)} + \sqrt{3}i\xi_{+1}m_{2,0}^{(d)},$$

$$\dot{m}_{2,2}^{(d)} = (-2i\xi_0 + \gamma_2)m_{2,2}^{(d)} + \sqrt{2}i\xi_{+1}m_{2,1}^{(d)}, \tag{B2}$$

with

$$\xi_0 = \left[\Omega + \frac{\sin\beta}{4} \Omega_p (e^{i\delta_p t} + e^{-i\delta_p t}) \right],$$

$$\xi_{-1} = \frac{\Omega_p}{4\sqrt{2}} [(1 + \cos\beta)e^{i\delta_p t} - (1 - \cos\beta)e^{-i\delta_p t}],$$

$$\xi_{+1} = \frac{\Omega_p}{4\sqrt{2}} [(1 - \cos\beta)e^{i\delta_p t} - (1 + \cos\beta)e^{-i\delta_p t}], \tag{B3}$$

where the coefficient γ_i $(i = 0, 1, 2)$ is the alignment relaxation rate in the dressed-state representation, which is mainly determined by the optical pump relaxation process [61] and the ground-state spin-exchange collision relaxation process [46] of the system. The monopole moment

B_0 : offset field B_{L1}: longitudinal fundamental wave
B_{L2}: longitudinal third harmonic B_T : transverse fundamental wave
B_p : probing field ε : light polarization k : light propagation
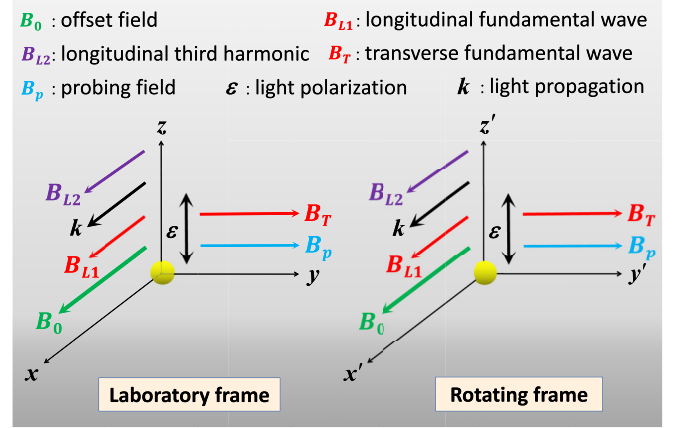
FIG. 7. Theoretical model geometry of scheme II with only one transverse rf field.

$m_{0,0}^{(d)}$ is an injection of the alignment, and the coefficient Γ_0 is the monopole moment relaxation rate related to the optical pump relaxation process. Considering the probing field is much weaker than the main fields, one can solve Eq. (B2) by using the perturbation approximation and Floquet method approach [62] with $m_{2,q}^{(d)}(t) = \sum_{l=-\infty}^{\infty} m_{2,q}^{(d)(l)}(t)e^{il\delta t}$, $q = -2, -1, 0, 1, 2$. The steady-state second-order perturbation solution of $m_{2,0}^{(d)}$ is then given by

$$m_{2,0}^{(d)} = -\frac{\Gamma_0}{3\gamma_0} + \frac{\Gamma_0 \gamma_1 \Omega_p^2}{16\gamma_0^2}$$

$$\times \left[\frac{(1-\cos\beta)^2}{\gamma_1^2 + (\delta_p + \Omega)^2} + \frac{(1+\cos\beta)^2}{\gamma_1^2 + (\delta_p - \Omega)^2} \right]. \tag{B4}$$

By performing the inverse rotation transformation on the steady-state solution, the time-independent component of $m_{2,0}$ in the laboratory frame xyz is given by

$$m_{2,0}^{(\text{dc})} = \frac{1 - 3\cos^2\beta}{4} m_{2,0}^{(d)}. \tag{B5}$$

APPENDIX C: SCHEME II WITH ONLY ONE TRANSVERSE rf FIELD

In the rotating frame $x'y'z'$ shown in Fig. 7, the physical quantities of the system in scheme II can be expressed as $\boldsymbol{B}_{x'} = [B_T \cos(\omega t + \varphi) + B_p \cos(\omega_p t)]\mathbf{e}_{x'}$ and $\boldsymbol{B}_{z'} = [B_0 + B_{L1}\cos(\omega t + \varphi) + B_{L2}\cos(3\omega t + \theta)]\mathbf{e}_{z'}$. Then the total Hamiltonian of the system is given by

$$H_{B_{\text{tot}}}^{(\text{II})} = H_{B_m}^{(\text{II})} + H_{B_p}^{(\text{II})}, \tag{C1}$$

with

$$H_{B_m}^{(\text{II})} = [\Omega_0 + \Omega_{L1}\cos(\omega t + \varphi) + \Omega_{L2}\cos(3\omega t + \theta)]F_0$$

$$+ \left[\frac{\Omega_T}{\sqrt{2}}\cos(\omega t + \varphi) \right](F_{-1} - F_{+1}), \tag{C2}$$

$$H_{B_p}^{(\text{II})} = \frac{\Omega_p}{\sqrt{2}}\cos(\omega_p t)(F_{-1} - F_{+1}), \tag{C3}$$
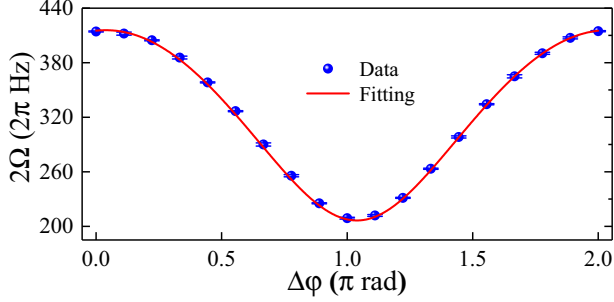
FIG. 8. Sideband interval in scheme II vs relative phase. The blue solid dots represent the measured data with a step of $\pi/9$. All data are measured under the resonance condition with $\Omega_0 = 2\pi \times 100.160$ kHz, $\Omega_{L1} = 2\pi \times 2.630(5)$ kHz, $\Omega_{L2} = 2\pi \times 8.040(5)$ kHz, and $\Omega_T = 2\pi \times 3.875(5)$ kHz. The red fitting curve is the theoretical fit of Eq. (C6).

where the symbol satisfies $\Omega_j = \mu_B g_F B_j (j=0, L_1, L_2, T, p)$. Following the effective Hamiltonian theory [52,53] and the rotating-wave approximation, the effective Hamiltonian of $H_{B_m}^{(II)}$ is given by

$$H_{B_m}^{(II)\text{eff}} \approx \Delta\Omega_0^{(II)} F_0 - \left[\Omega_R^{(II)} e^{i(\delta_R t + \theta - \varphi)} + \Omega_C^{(II)} e^{i(\delta_C t + 2\varphi)}\right] F_{-1}$$
$$+ \left[\Omega_R^{(II)} e^{-i(\delta_R t + \theta - \varphi)} + \Omega_C^{(II)} e^{-i(\delta_C t + 2\varphi)}\right] F_{+1}, \quad (C4)$$

with

$$\Delta\Omega_0^{(II)} = \frac{\Omega_0 \Omega_T^2}{4(\Omega_0^2 - \omega^2)}, \quad \Omega_R^{(II)} = \frac{\Omega_{L1} \Omega_T}{12\sqrt{2}\omega},$$

$$\Omega_C^{(II)} = \frac{\Omega_{L2} \Omega_T}{4\sqrt{2}\omega}. \quad (C5)$$

After diagonalization of the effective Hamiltonian $H_{B_m}^{(II)\text{eff}}$, the AT splitting of scheme II can be given by

$$\Omega^{(II)} = \sqrt{\Omega_z^{(II)2} + 2\left(\Omega_R^{(II)2} + \Omega_C^{(II)2} + 2\Omega_R^{(II)}\Omega_C^{(II)} \cos\Delta\phi\right)}, \quad (C6)$$

where $\Omega_z^{(II)} = \Delta\Omega_0^{(II)} + \Omega_0 - 2\omega$ and $\Delta\Omega_0^{(II)}$ is the ac Zeeman shift of the system in scheme II. The relative phase still satisfies $\Delta\phi = \theta - 3\varphi$.

The experimental setup of scheme II is basically the same as that of scheme I. The only difference is that there are two pairs of Helmholtz coils in scheme II, corresponding to the generation of the transverse rf field $\boldsymbol{B}_T$ and probing field $\boldsymbol{B}_p$, and the outer solenoid coils are two layers, corresponding to the generation of the longitudinal rf fields $\boldsymbol{B}_{L1}$ and $\boldsymbol{B}_{L2}$ shown in Fig. 3.

Under the resonance condition with $\frac{\Delta\Omega_0^{(II)}}{2\pi} \approx 50$ Hz, the variation trend of the sideband interval with $\Delta\phi$ is shown in Fig. 8. The regulation of AT splitting by the relative phase appears to be out of phase compared to that in scheme I. Since the Rabi frequency determining the ac Zeeman shift of the system is related to only the transverse component, the ac Zeeman shift in scheme II cannot be canceled completely.

According to Eqs. (C5) and (C6), there is only the transverse rf component linearly regulating AT splitting at any relative phase. However, since the variation of the transverse rf component will change the ac Zeeman shift of the
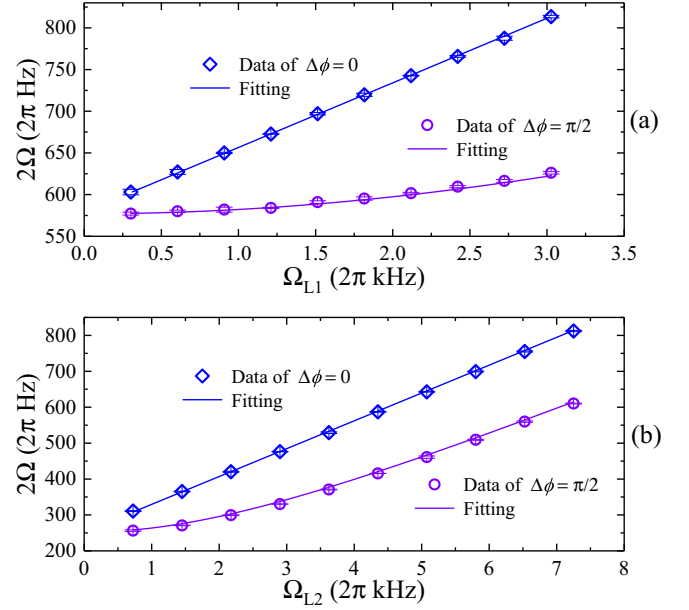

FIG. 9. Sideband interval vs longitudinal Rabi frequency. The blue diamonds represent the measured data with $\Delta\phi = 0$; the purple circles represent the measured data with $\Delta\phi = \pi/2$. (a) is the measurement under the fitting value of $\Omega_{L2} = 2\pi \times 7.480(5)$ kHz; (b) is the measurement under the fitting value of $\Omega_{L1} = 2\pi \times 3.256(5)$ kHz. All data are measured under resonance conditions with $\Omega_0 = 2\pi \times 100.110$ kHz, $\Omega_T = 2\pi \times 7.750(5)$ kHz, and $\frac{\Delta\Omega_0^{(II)}}{2\pi} \approx 200$ Hz. The fitting curves are the theoretical fits of Eq. (C6).

system, the equivalent Larmor precession frequency of the two-photon resonance will also be changed. When the initial frequencies ω and 3ω resonant with the system are determined and fixed, the transverse rf component and the AT splitting do not satisfy the linear relationship because once the transverse rf component changes, $\Omega_z^{(II)}$ in Eq. (C6) will also be changed, and the original linear relationship will be broken. Therefore, in the actual measurement, it is difficult to satisfy the linear relationship between the transverse rf component and the AT splitting in scheme II. For the longitudinal rf fields in scheme II, only with the condition of $\Delta\phi = 0$ or π can the linear relationship between each longitudinal rf component and the AT splitting be satisfied, as shown in Fig. 9.

In fact, scheme I and scheme II include two manners for measuring the longitudinal rf component based on a single two-photon process. It is necessary to retain only the rf magnetic fields that generate a single Raman process or cascade process with a weak transverse rf field probing; using the sideband interval of the AT doublet, the linear measurement of the longitudinal rf component can also be achieved. Although the linear measurement based on a single two-photon process is not affected by the relative phase, it also has the defect that the ac Zeeman shift of the system cannot be canceled completely.

In terms of measuring the relative phase of the rf field, scheme I and scheme II are essentially the same with an equivalent measurement effect. That is, both of them measure the rf phase by using the AT splitting induced by the

interference field between the effective field Ω_C of the cascade two-photon process and the effective field Ω_R of the Raman two-photon process. Due to the existence of the transverse rf field, both scheme I and scheme II will inevitably bring ac Zeeman shift to the system. The difference is that scheme I can use the amplitude ratio between the two transverse rf fields to eliminate the ac Zeeman shift of the system, but scheme II cannot. In addition, since there is only one longitudinal rf field in scheme I, the longitudinal Rabi frequency Ω_L is the greatest common divisor of the AT splitting Ω according to Eqs. (5) and (6). Thus, the amplitude measurement of the longitudinal rf field in scheme I does not depend on the relative phase $\Delta\phi$ and meets the requirements of linear measurement.

[1] D. A. Anderson, R. E. Sapiro, and G. Raithel, IEEE Aerospace Electron. Syst. Mag. **35**, 48 (2020).

[2] A. K. Robinson, N. Prajapati, D. Senic, M. T. Simons, and C. L. Holloway, Appl. Phys. Lett. **118**, 114001 (2021).

[3] J. A. Sedlacek, A. Schwettmann, H. Kübler, R. Löw, T. Pfau, and J. P. Shaffer, Nat. Phys. **8**, 819 (2012).

[4] C. L. Holloway, J. A. Gordon, S. Jefferts, A. Schwarzkopf, D. A. Anderson, S. A. Miller, N. Thaicharoen, and G. Raithel, IEEE Trans. Antennas Propag. **62**, 6169 (2014).

[5] J. A. Gordon, C. L. Holloway, A. Schwarzkopf, D. A. Anderson, S. Miller, N. Thaicharoen, and G. Raithel, Appl. Phys. Lett. **105**, 024104 (2014).

[6] C. L. Holloway, M. T. Simons, J. A. Gordon, P. F. Wilson, C. M. Cooke, D. A. Anderson, and G. Raithel, IEEE Trans. Electromagn. Compat. **59**, 717 (2017).

[7] D. A. Anderson, R. E. Sapiro, and G. Raithel, IEEE Trans. Antennas Propag. **69**, 2455 (2021).

[8] F.-D. Jia, H.-Y. Zhang, X.-B. Liu, J. Mei, Y.-H. Yu, Z.-Q. Lin, H.-Y. Dong, Y. Liu, J. Zhang, F. Xie, and Z.-P. Zhong, J. Phys. B **54**, 165501 (2021).

[9] H. Fan, S. Kumar, J. Sheng, J. P. Shaffer, C. L. Holloway, and J. A. Gordon, Phys. Rev. Appl. **4**, 044015 (2015).

[10] C. L. Holloway, M. T. Simons, M. D. Kautz, A. H. Haddab, J. A. Gordon, and T. P. Crowley, Appl. Phys. Lett. **113**, 094101 (2018).

[11] J. A. Sedlacek, A. Schwettmann, H. Kübler, and J. P. Shaffer, Phys. Rev. Lett. **111**, 063001 (2013).

[12] C. L. Holloway, N. Prajapati, A. B. Artusio-Glimpse, S. Berweger, M. T. Simons, Y. Kasahara, A. Alù, and R. W. Ziolkowski, Appl. Phys. Lett. **120**, 204001 (2022).

[13] J. A. Gordon, M. T. Simons, A. H. Haddab, and C. L. Holloway, AIP Adv. **9**, 045030 (2019).

[14] M. T. Simons, M. D. Kautz, C. L. Holloway, D. A. Anderson, G. Raithel, D. Stack, M. C. St. John, and W. Su, J. Appl. Phys. **123**, 203105 (2018).

[15] C. Holloway, M. Simons, A. H. Haddab, J. A. Gordon, D. A. Anderson, G. Raithel, and S. Voran, IEEE Antennas Propag. Mag. **63**, 63 (2021).

[16] M. T. Simons, A. H. Haddab, J. A. Gordon, D. Novotny, and C. L. Holloway, IEEE Access **7**, 164975 (2019).

[17] L. G. Spitler, P. Scholz, J. W. T. Hessels, S. Bogdanov, A. Brazier, F. Camilo, S. Chatterjee, J. M. Cordes, F. Crawford, J. Deneva, R. D. Ferdman, P. C. C. Freire, V. M. Kaspi, P. Lazarus, R. Lynch, E. C. Madsen, M. A. McLaughlin, C. Patel, S. M. Ransom, A. Seymour, I. H. Stairs, B. W. Stappers, J. van Leeuwen, and W. W. Zhu, Nature (London) **531**, 202 (2016).

[18] D. E. Alsdorf, J. M. Melack, T. Dunne, L. A. K. Mertes, L. L. Hess, and L. C. Smith, Nature (London) **404**, 174 (2000).

[19] U. L. Rohde, J. C. Whitaker, and H. Zahnd, *Communications Receivers: Principles and Design* (McGraw-Hill Education, New York, 2017)

[20] H. Maeda, D. V. L. Norum, and T. F. Gallagher, Science **307**, 1757 (2005).

[21] M. Y. Jing, Y. Hu, J. Ma, H. Zhang, L. J. Zhang, L. T. Xiao, and S. T. Jia, Nat. Phys. **16**, 911 (2020).

[22] M. T. Simons, A. H. Haddab, J. A. Gordon, and C. L. Holloway, Appl. Phys. Lett. **114**, 114101 (2019).

[23] L. Lin, Y. He, Z. Yin, D. Li, Z. Jia, Y. Zhao, B. Chen, and Y. Peng, Appl. Opt. **61**, 1427 (2022).

[24] M. Fleischhauer, A. Imamoglu, and J. P. Marangos, Rev. Mod. Phys. **77**, 633 (2005).

[25] D. Shylla and K. Pandey, arXiv:1802.09935.

[26] D. Shylla, E. O. Nyakang'o, and K. Pandey, Sci. Rep. **8**, 8692 (2018).

[27] D. A. Anderson, R. E. Sapiro, L. F. Gonçalves, R. Cardman, and G. Raithel, Phys. Rev. Appl. **17**, 044020 (2022).

[28] H. Sun, S. Yong, and J. C. Sharp, J. Magn. Reson. **299**, 135 (2019).

[29] X. Wang, D. Hernando, and S. B. Reeder, Magn. Reson. Med. **84**, 609 (2020).

[30] J. Wen, A. L. Sukstanskii, and D. A. Yablonskiy, Magn. Reson. Med. **80**, 101 (2018).

[31] H. Cline, R. Mallozzi, Z. Li, G. McKinnon, and W. Barber, Magn. Reson. Med. **51**, 1129 (2004).

[32] L. I. Sacolick, F. Wiesinger, I. Hancu, and M. W. Vogel, Magn. Reson. Med. **63**, 1315 (2010).

[33] G. R. Morrell, Magn. Reson. Med. **60**, 889 (2008).

[34] W. Chen, A. Takahashi, and E. Han, Magn. Reson. Imaging **29**, 608 (2011).

[35] D. Budker, D. F. Kimball, and D. P. DeMille, *Atomic Physics* (Oxford University Press, New York, 2008).

[36] A. P. Hilton, C. Perrella, A. N. Luiten, and P. S. Light, Phys. Rev. Appl. **11**, 024065 (2019).

[37] G. S. Agarwal, T. N. Dey, and D. J. Gauthier, Phys. Rev. A **74**, 043805 (2006).

[38] X.-X. Geng, G.-Q. Yang, P.-L. Qi, W.-W. Tang, S.-Q. Liang, G.-X. Li, and G.-M. Huang, Phys. Rev. A **103**, 053112 (2021).

[39] M. Baur, S. Filipp, R. Bianchetti, J. M. Fink, M. Göppl, L. Steffen, P. J. Leek, A. Blais, and A. Wallraff, Phys. Rev. Lett. **102**, 243602 (2009).

[40] T. Hönigl-Decrinis, R. Shaikhaidarov, S. E. de Graaf, V. N. Antonov, and O. V. Astafiev, Phys. Rev. Appl. **13**, 024066 (2020).

[41] A. Weis, J. Wurster, and S. I. Kanorsky, J. Opt. Soc. Am. B **10**, 716 (1993).

[42] S. I. Kanorsky, A. Weis, J. Wurster, and T. W. Hänsch, Phys. Rev. A **47**, 1220 (1993).

[43] A. Weis, G. Bison, and A. S. Pazgalev, Phys. Rev. A **74**, 033401 (2006).

[44] D. Sheng, S. Li, N. Dural, and M. V. Romalis, Phys. Rev. Lett. **110**, 160802 (2013).

[45] Y. Shi and A. Weis, Eur. Phys. J. D **72**, 73 (2018).

[46] T. Scholtes, S. Pustelny, S. Fritzsche, V. Schultze, R. Stolz, and H.-G. Meyer, Phys. Rev. A **94**, 013403 (2016).

[47] G. Yang, H. Zhang, X. Geng, S. Liang, Y. Zhu, J. Mao, G. Huang, and G. Li, Opt. Express **26**, 30313 (2018).

[48] E. Breschi and A. Weis, Phys. Rev. A **86**, 053427 (2012).

[49] S. J. Ingleby, C. O'Dwyer, P. F. Griffin, A. S. Arnold, and E. Riis, Phys. Rev. Appl. **10**, 034035 (2018).

[50] G. Di Domenico, H. Saudan, G. Bison, P. Knowles, and A. Weis, Phys. Rev. A **76**, 023407 (2007).

[51] D. A. Varshalovich, A. N. Moskalev, and V. K. Khersonskii, *Quantum Theory of Angular Momentum* (World Scientific, Singapore, 1988).

[52] W. Shao, C. Wu, and X.-L. Feng, Phys. Rev. A **95**, 032124 (2017).

[53] R. Tan, G.-X. Li, and Z. Ficek, Phys. Rev. A **78**, 023833 (2008).

[54] C. Cohen-Tannoudji, J. Dupont-Roc, and G. Grynberg, *Atom-Photon Interactions: Basic Process and Appilcations* (Wiley-VCH, Weinheim, 2004).

[55] Z. Liang, X.-X. Geng, P.-L. Qi, K. Jin, G.-Q. Yang, G.-X. Li, and G.-M. Huang, Opt. Express **29**, 33197 (2021).

[56] H.-T. Zhou, D.-W. Wang, D. Wang, J.-X. Zhang, and S.-Y. Zhu, Phys. Rev. A **84**, 053835 (2011).

[57] L. Margalit, M. Rosenbluh, and A. D. Wilson-Gordon, Phys. Rev. A **87**, 033808 (2013).

[58] S. J. Ingleby, C. O'Dwyer, P. F. Griffin, A. S. Arnold, and E. Riis, Phys. Rev. A **96**, 013429 (2017).

[59] S. Haroche and F. Hartmann, Phys. Rev. A **6**, 1280 (1972).

[60] K. Blum, *Density Matrix Theory and Applications* (Plenum Press, New York, 1981).

[61] M. Auzinsh, D. Budker, and S. Rochester, *Optically Polarized Atoms: Understanding Light-Atom Interactions* (Oxford University Press, New York, 2010).

[62] Z. Ficek and R. Tanaś, *Quantum-Limit Spectroscopy*, Springer Series in Optical Sciences Vol. 200 (Springer, New York, 2017), pp. 39–72.